Journal of Coastal Research	21	6	1257–1268	West Palm Beach, Florida	November 2005

ICEM: Integrated Coastal Engineering Model

Usama M. Saied and Ioannis K. Tsanis

Department of Civil Engineering
McMaster University
1280 Main Street West
Hamilton, ON L8S 4R7, Canada

ABSTRACT

SAIED, U.M. and TSANIS, I.K., 2005. ICEM: Integrated Coastal Engineering Model. *Journal of Coastal Research,* 21(6), 1257–1268. West Palm Beach (Florida), ISSN 0749-0208.

A morphodynamical model for coastal areas has been developed by simultaneously simulating the dynamics of waves, coastal currents, and sediment transport rates. The sediment transport rates are calculated on a staggered two-dimensional grid, and then the sediment budget is used to predict the coastal morphology changes. The model can simulate short-term and long-term morphological changes around coastal structures. A case study along the Nile Delta coast in Egypt is used to demonstrate the effectiveness of the present model by calibrating and verifying the model results with field measurements. The model can be applied to coastal domains with similar characteristics with appropriate parameter calibration.

ADDITIONAL INDEX WORDS: *Beach deformation, coastal structures, shoreline change, morphological modeling.*

INTRODUCTION

Shoreline change models are used to predict shoreline changes associated with coastal structures or storm effects over the long term. These models are based on the single line or multiple line theories, where the potential long shore and cross shore sediment transport components are calculated empirically for the open shore case. These models have the advantage of being very fast, and they can predict long-term shoreline changes very well after suitable calibration. However, they cannot accurately predict the impact of morphological changes in the vicinity of coastal structures that are due to short-term storms. An alternative approach involves the modeling of the whole suite of elementary processes responsible for the local morphological changes in a given area (LEONT'YEV, 1999). A typical coastal area model consists of several modules describing the wave field, the spatial distribution of wave-induced currents, the associated sediment transport fluxes, and finally the resulting spatial and temporal changes of the bed level. Such an approach is employed in the models developed by Delft Hydraulics (DE VRIEND *et al.,* 1993; ROELVINK, RENIERS, and WALSTRA, 1995), Danish Hydraulic Institute (BROKER, 1995; BROKER *et al.*, 1995), or HR Wallingford (PRICE, CHESHER, and SOUTHGATE, 1995). The attempts to evaluate the short-term morphological impacts of coastal structures using these models are not yet numerous, but the results obtained are encouraging. Although these models can be used to predict medium-term morphological impacts on coastal structures, the long-term morphological impacts are still predicted solely by the shoreline models.

In this paper an integrated coastal engineering model (ICEM) is presented, which simultaneously simulates the dynamics of the waves, the coastal circulation, and the rate of bed level changes. The ICEM is capable of modeling both the short- and long-term bathymetric changes due to the presence of coastal structures, and its capabilities are illustrated in several test cases. A case study in Ras El-Bar along the Nile Delta coast in Egypt is used to calibrate and verify the ICEM.

DOI:10.2112/04-0188.1 received 24 March 2004; accepted in revision 20 July 2004.

MODEL DESCRIPTION

The model consists of three main modules: the wave transformation module, the coastal circulation module, and the sediment transport and morphological module. First, the wave transformation module transforms the offshore monochromatic representative wave over a two-dimensional grid, which covers the whole coastal domain. With the wave information available over the two-dimensional grid, the circulation model calculates the corresponding wave forcing and simulates the coastal currents marching in time until it reaches the steady state. Finally, both wave and current information are passed to the sediment transport and morphological module, which calculates the sediment fluxes over a staggered two-dimensional grid and then calculates the morphological changes, imposing the necessary boundary conditions for the structures. The waves, currents, and sediment transport rates are recalculated at every so-called morphological time step Δt_m. The morphological time step is determined by the most rapid bathymetric evolution inside the model area and is automatically calculated by the model. Figure 1 shows the model structure.

Wave Transformation Module

This module employs either a parabolic or an elliptic water wave transformation model. The elliptic water wave trans-

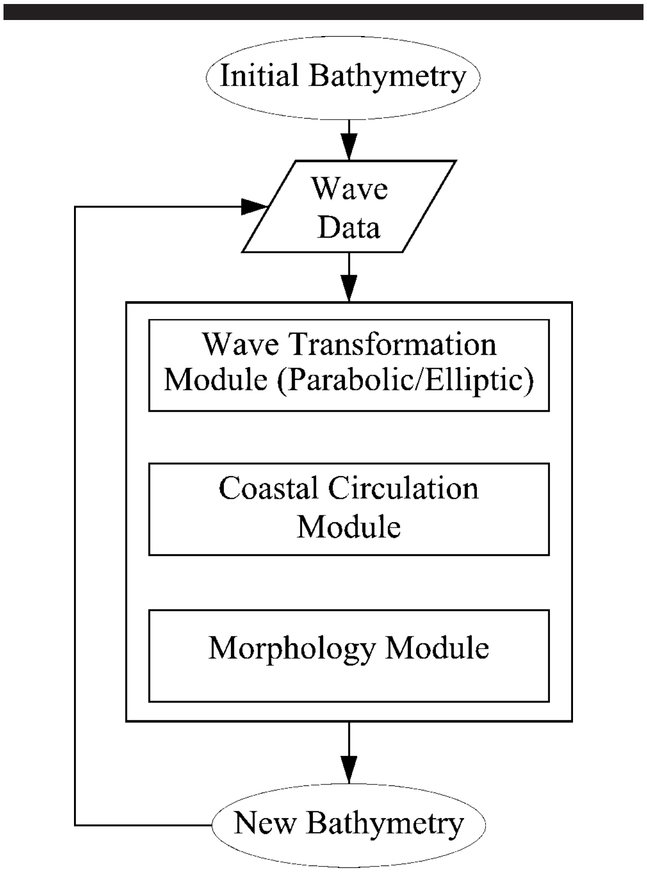

Figure 1. ICEM model structure.

formation model solves the mild slope equation directly, which was developed by BERKHOFF (1972). This model can simulate wave diffraction, refraction, shoaling, and reflection. It employs the generalized conjugate gradient scheme to solve the resulting system matrix (SAIED and TSANIS, 2004). Although it is accurate and unconditionally stable, it is computationally time consuming. Therefore, in real cases, the parabolic model is preferred, which is essentially a rational approximation to the original elliptic mild slope equation. The parabolic model developed by SAIED and TSANIS (2005) is incorporated into the integrated model, which is based on the [1/1] generalized Padé approximation. This model can simulate very wide wave angles up to 70° (SAIED and TSANIS, 2005). The parabolic model, however, cannot simulate the wave reflection from structures. The ICEM uses the parabolic model and has the option of refining the parabolic solution with the elliptic model for certain user-specified areas, where reflections are expected to cause significant change.

Coastal Circulation Module

The coastal circulation module employs time-dependent two-dimensional depth-averaged Navier-Stocks equations. The model can simulate currents driven by wind, waves, Coriolis effects, and wave rolling in the surf zone. The governing equations can be written as:

$$\frac{\partial \eta}{\partial t} + \frac{\partial (h + \eta)u}{\partial x} + \frac{\partial (h + \eta)v}{\partial y} = 0, \tag{1}$$

$$\frac{\partial u}{\partial t} + u\frac{\partial u}{\partial x} + v\frac{\partial u}{\partial y} = -g\frac{\partial \eta}{\partial x} + \varepsilon\left(\frac{\partial^2 u}{\partial x^2} + \frac{\partial^2 u}{\partial y^2}\right) + C_x u + B_x, \tag{2}$$

$$\frac{\partial v}{\partial t} + u\frac{\partial v}{\partial x} + v\frac{\partial v}{\partial y} = -g\frac{\partial \eta}{\partial y} + \varepsilon\left(\frac{\partial^2 v}{\partial x^2} + \frac{\partial^2 v}{\partial y^2}\right) + C_y v + B_y, \tag{3}$$

where η is the water surface elevation, h is the water depth, u and v are the depth-averaged velocity components, ϵ is the eddy viscosity, C_x and B_x define a linear source term for the x-momentum equation, and C_y and B_y define a linear source term for the y-momentum equation. The source term can include the radiation stresses, Coriolis forces, and bed friction. The eddy viscosity ϵ is given by HORIKAWA (1988) after LONGUET-HIGGINS (1970) as follows:

$$\epsilon = N l_{SL}\sqrt{g(h + \eta)}, \tag{4}$$

where N is a constant whose value is deduced to be smaller than 0.016 and l_{SL} is the distance measured from the shoreline to the point of interest. The bed friction term can be given by LEONT'YEV (1999), after LE BLOND and TANG (1974), as follows:

$$\tau_{bx} = \frac{2}{\pi}C_f \rho u_{bm}[(1 + \cos^2\theta)u + v \sin\theta \cos\theta], \tag{5}$$

$$\tau_{by} = \frac{2}{\pi}C_f \rho u_{bm}[(1 + \sin^2\theta)v + u \sin\theta \cos\theta], \tag{6}$$

where τ_{bx} and τ_{by} are the bed shear stresses in the x and y directions, respectively; C_f is the dimensionless bed friction coefficient, which is usually of the order of 0.01; θ is the wave angle with respect to the x-axis; and u_{bm} is the maximum bottom orbital velocity, which can be obtained from the linear wave theory as follows:

$$u_{bm} = \frac{\omega H}{2\sinh(kh)}, \tag{7}$$

where k is the wave number, H is the wave height, and ω is the wave angular frequency.

Equations (5) and (6) contribute to the source term in Equations (2) and (3) as follows:

$$C_x = \left(\frac{-2}{\pi}\frac{C_f u_m}{h_w}\right)(1 + \cos^2\theta),$$

$$B_x = \left(\frac{-2}{\pi}\frac{C_f u_m}{h_w}\right)v^*\sin\theta\cos\theta,$$

$$C_y = \left(\frac{-2}{\pi}\frac{C_f u_m}{h_s}\right)(1 + \sin^2\theta),$$

$$B_x = \left(\frac{-2}{\pi}\frac{C_f u_m}{h_s}\right)u^*\sin\theta\cos\theta, \tag{8}$$

where h_w and h_s are the water depths at the points where the x and y components of the velocity are calculated, respectively, and u^* and v^* are the x- and y-components of the velocity at the points where the y and x velocity components are calculated, respectively. The forcing due to waves can be obtained from (LEONT'YEV, 1999)

$$F_x = \frac{\partial}{\partial x}(S_{xx} + R_{xx}) + \frac{\partial}{\partial y}(S_{xy} + R_{xy}),$$

$$F_y = \frac{\partial}{\partial y}(S_{yy} + R_{yy}) + \frac{\partial}{\partial x}(S_{yx} + R_{yx}), \tag{9}$$

where S_{ij} is the radiation stress tensor and R_{ij} are the stresses due to rollers in breaking waves (DALLY and OSIECKI, 1994). The radiation stresses are given by

$$S_{xx} = \frac{E}{2}[2n(1 + \cos^2\theta) - 1] - \frac{\rho M_{Wx}^2}{h},$$

$$S_{yy} = \frac{E}{2}[2n(1 + \sin^2\theta) - 1] - \frac{\rho M_{Wy}^2}{h},$$

$$S_{xy} = S_{yx} = \frac{E}{2}n \sin 2\theta - \frac{\rho M_{Wx} M_{Wy}}{h}, \tag{10}$$

where $E = \rho g H^2/8$ is the wave energy per unit area, $n = c_g/c$ is the wave index, and M_{Wx} and M_{Wy} are water discharges that represent the onshore mass flux caused by waves (Stokes drift) and rollers:

$$(M_{Wx}, M_{Wy}) = (E + E_r)(\cos\theta, \sin\theta)/\rho c, \tag{11}$$

In Equation (11), E_r is the roller energy per unit area, which is defined as follows:

$$E_r = 4\beta_r \frac{c}{gT}\left(\frac{H}{\gamma h}\right)E, \tag{12}$$

where $\beta_r \approx 0.9$, c is the wave celerity, and γ is the breaking constant. The stresses due to rollers are given by:

$$R_{xx} = 2E_r\cos^2\theta, \qquad R_{yy} = 2E_r\sin^2\theta,$$

$$R_{xy} = R_{yx} = E_r\sin 2\theta. \tag{13}$$

The forcing due to the waves given by Equation (9) and the Coriolis forces contributes to the source term in Equations (2) and (3) as follows:

$$B_x = \frac{-1}{h_w\rho}F_x + C_r v^*, \qquad B_y = \frac{-1}{h_s\rho}F_y - C_r u^*, \tag{14}$$

where $C_r = 2\pi \sin\phi/(24 \times 3{,}600)$ is the Coriolis parameter, ϕ is the mean geographic latitude at the area, and the x- and y-axis directions are from north to south and from west to east, respectively.

Boundary Conditions

A no-flow boundary condition is imposed on the boundaries along islands, shorelines, and breakwaters. At the lateral open boundaries, uniform flow is assumed:

$$\frac{\partial u}{\partial y} = 0.0, \qquad \frac{\partial v}{\partial y} = 0.0. \tag{15}$$

In order for Equation (15) to be correct, the domain has to be extended laterally so that uniform conditions are satisfied. At the offshore boundary, a no-flow boundary condition is applied.

Numerical Scheme

The coastal domains considered in this analysis are usually relatively large domains. This makes the direct solution of Equations (1) to (3) cumbersome because of the large system matrix. Therefore, the alternating directional implicit (ADI) scheme was chosen to discretize the governing equations. The discretization was done so that the boundary conditions could be implemented easily. Therefore, the continuity and momentum equations are solved uncoupled so that Equation (15) could be implemented as a lateral boundary condition. The uncoupling of the equations leads to a discretization, which is conditionally stable according to:

$$\Delta t \le \frac{2\min(\Delta x, \Delta y)}{\sqrt{2gh_{\max}}}, \tag{16}$$

where Δt is the time step and Δx and Δy are the grid sizes in the x and y directions, respectively. An ADI discretization that solves the continuity and the momentum equations simultaneously is usually unconditionally stable. However, it loses its accuracy for Courant numbers higher than 4 (SHEN, 1991). In addition, Equation (15) cannot be implemented as a lateral boundary condition unless the matrix is solved by a method other than the double sweep method, which loses the advantage of the ADI scheme. The current scheme, although conditionally stable, can work with Courant numbers up to 2 without any loss of accuracy, as will be shown in the sensitivity analysis.

The time step is split into two fractional steps. In the first fractional step, the equations are solved sweeping in x direction. In the second fractional step, the equations are solved sweeping in y direction. For the first fractional time step, Equation (1) is discretized as follows:

$$\frac{\eta^n - \eta^o}{\Delta t/2} + \frac{u_e^o(h_e + \eta_e^n) - u_w^o(h_w + \eta_w^n)}{\Delta x} + \frac{v_n^o(h_n + \eta_n^o) - v_s^o(h_s + \eta_s^o)}{\Delta y} = 0, \tag{17}$$

where the superscripts n represent the values at the current time step and the superscripts o represent the known values from the old time step. The subscripts e, w, s, and n represent the values at the east, west, south and north faces of the control volume as shown in Figure 2. The values at the faces can be linearly interpolated as follows:

$$\eta_e = \frac{\eta_E + \eta_P}{2}, \qquad \eta_w = \frac{\eta_W + \eta_P}{2},$$

$$\eta_n = \frac{\eta_N + \eta_P}{2}, \qquad \eta_s = \frac{\eta_S + \eta_P}{2}, \tag{18}$$

where the subscripts E, W, S, and N represent the values at the discrete points, as shown in Figure 2. Equations (17) and (18) can be written in the form of linear discrete equations as follows:

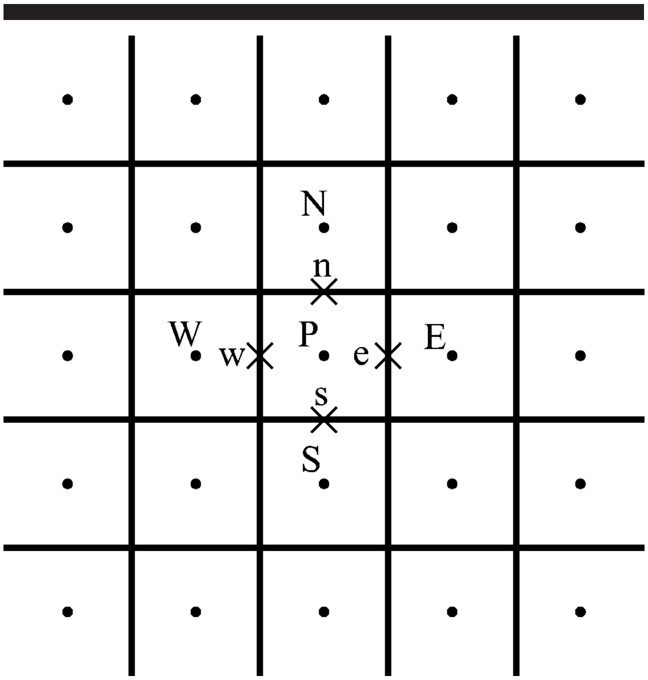

Figure 2. Definition of grid points.

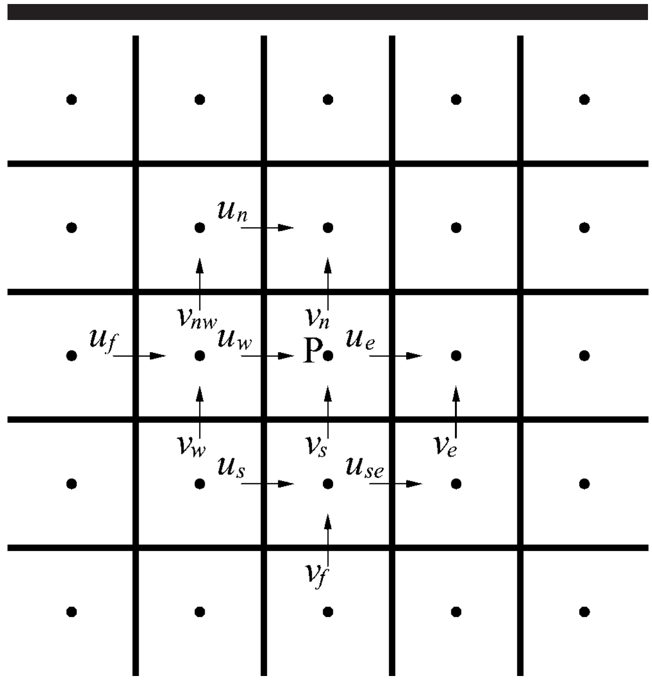

Figure 3. Definition of velocity components.

$$
\begin{aligned}
a_P\eta_P^n &= a_W\eta_W^n + a_E\eta_E^n + b,\\
a_P &= \frac{2}{\Delta t} + \frac{u_e^o - u_w^o}{2\Delta x},\\
a_E &= -\frac{u_e^o}{2\Delta x}, \qquad a_W = \frac{u_w^o}{2\Delta x},\\
b &= \frac{2}{\Delta t}\eta_P^o - \frac{u_e^o h_e - u_w^o h_w}{\Delta x} - \frac{v_n^o h_n - v_s^o h_s}{\Delta y}\\
&\quad - \frac{v_n^o(\eta_N^o + \eta_P^o) - v_s^o(\eta_S^o + \eta_P^o)}{2\Delta y}.
\end{aligned}
\tag{19}
$$

Similarly, for the second fractional time step, the linear discrete equations that describe Equation (1) can be written as follows:

$$
\begin{aligned}
a_P\eta_P^n &= a_S\eta_S^n + a_N\eta_N^n + b,\\
a_P &= \frac{2}{\Delta t} + \frac{v_n^o - v_s^o}{2\Delta y},\\
a_N &= -\frac{v_n^o}{2\Delta y}, \qquad a_S = \frac{v_s^o}{2\Delta y},\\
b &= \frac{2}{\Delta t}\eta_P^o - \frac{v_n^o h_n - v_s^o h_s}{\Delta y} - \frac{u_e^o h_e - u_w^o h_w}{\Delta x}\\
&\quad - \frac{u_e^o(\eta_E^o + \eta_P^o) - u_w^o(\eta_o W + \eta_P^o)}{2\Delta x}.
\end{aligned}
\tag{20}
$$

For the first fractional time step, Equation (2) is discretized as follows:

$$
\begin{aligned}
&\frac{u_w^n - u_w}{\Delta t/2} + u_w\frac{u_P^n - u_W^n}{\Delta x} + v^*\frac{u_n - u_s}{2\Delta y}\\
&\quad = -g\frac{\eta_P^n - \eta_W^n}{\Delta x} + \varepsilon\frac{u_e^n - 2u_w^n + u_f^n}{\Delta x^2}\\
&\quad\quad + \varepsilon\frac{u_n - 2u_w + u_s}{\Delta y^2} + C_x u_w^n + B_x,
\end{aligned}
\tag{21}
$$

where the superscripts *o,* which indicate the old values, have been removed for convenience, and u_w, u_e, u_f, u_n, u_s, v_s, v_w, v_n, and v_{nw} are defined in Figure 3.

The derivative in the second term in Equation (21) (the advective term) is defined in terms of the values of the velocities at the discrete points. However, the velocities are defined at the control volume faces. Therefore, an approximation of the values of velocities at the discrete points in terms of the velocities at the faces is proposed as follows:

$$
\begin{aligned}
u_P &= u_w\left(\frac{\alpha + 1}{2}\right) + u_e\left(\frac{1 - \alpha}{2}\right) \quad \text{and}\\
u_W &= u_f\left(\frac{\alpha + 1}{2}\right) + u_w\left(\frac{1 - \alpha}{2}\right),
\end{aligned}
\tag{22}
$$

where the value of α at the faces of the control volumes is given as a function of the grid Peclet number Pe_Δ. The Peclet number is the ratio between the advection and the diffusion, which can be defined as follows:

$$
Pe_\Delta = \frac{u\Delta x}{\varepsilon},
\tag{23}
$$

where u is the local velocity and Δx is the grid spacing. Solving the one-dimensional advection-diffusion problem results in the following expression for α:

$$\alpha = 1 - \frac{2[\exp(Pe_\Delta) - 1]}{\exp(Pe_\Delta) - 1}. \tag{24}$$

If the problem is advection dominated (*i.e., $Pe_\Delta \to \infty$*), the value of α tends to unity, which leads to the upwinding difference scheme, as defined by Equation (24). On the other hand, if the problem is diffusion dominated (*i.e., $Pe_\Delta \to 0$*), α tends to be zero, which leads to the central differencing scheme. The calculation of the exponent in Equation (24), however, is computationally expensive. Therefore, the following approximation is used instead of Equation (24):

$$\alpha = \frac{(Pe_\Delta)^2}{5 + (Pe_\Delta)^2}, \tag{25}$$

which has the same limiting characteristics as Equation (24).

Equations (21) and (22) can be written in the following linear form:

$$\begin{aligned}
a_P u_w^n &= a_E u_e^n + a_W u_f^n + b,\\
a_P &= \frac{2}{\Delta t} + \frac{2\varepsilon}{\Delta x^2} - C_x + \frac{u_w \alpha}{\Delta x},\\
a_E &= \frac{\varepsilon}{\Delta x^2} - \frac{u_w(1 - \alpha)}{2\Delta x},\\
a_W &= \frac{\varepsilon}{\Delta x^2} + \frac{u_w(1 + \alpha)}{2\Delta x},\\
b &= \frac{2}{\Delta t} u_w - v^* \frac{u_n - u_s}{2\Delta y} - g\frac{\eta_P^n - \eta_W^n}{\Delta x}\\
&\quad + \varepsilon \frac{u_n - 2u_w + u_s}{\Delta y^2} + B_x,
\end{aligned} \tag{26}$$

where α is given by Equation (25) and Pe_Δ is given by Equation (23) with $u = u_w$. Similarly, for the second fractional time step, the linear discrete equations that describe Equation (2) can be written as follows:

$$\begin{aligned}
a_P u_w^n &= a_N u_n^n + a_S u_s^n + b,\\
a_P &= \frac{2}{\Delta t} + \frac{2\varepsilon}{\Delta y^2} - C_x + \frac{v^* \alpha}{\Delta y},\\
a_N &= \frac{\varepsilon}{\Delta y^2} - \frac{v^*(1 - \alpha)}{2\Delta y},\\
a_S &= \frac{\varepsilon}{\Delta y^2} + \frac{v^*(1 + \alpha)}{2\Delta y},\\
b &= \frac{2}{\Delta t} u_w - u_w \frac{u_e - u_f}{2\Delta x} - g\frac{\eta_P^n - \eta_W^n}{\Delta x}\\
&\quad + \varepsilon \frac{u_e - 2u_w + u_f}{\Delta x^2} + B_x,
\end{aligned} \tag{27}$$

where α is given by Equation (25) and Pe_Δ is given by:

$$Pe_\Delta = \frac{v^* \Delta y}{\varepsilon}. \tag{28}$$

Using the same procedure, the linear discrete equations that describe Equation (3) for the first fractional time step can be written as follows:

$$\begin{aligned}
a_P v_s^n &= a_E v_e^n + a_W v_w^n + b,\\
a_P &= \frac{2}{\Delta t} + \frac{2\varepsilon}{\Delta x^2} - C_y + \frac{u^* \alpha}{\Delta x},\\
a_E &= \frac{\varepsilon}{\Delta x^2} - \frac{u^*(1 - \alpha)}{2\Delta x},\\
a_W &= \frac{\varepsilon}{\Delta x^2} + \frac{u^*(1 + \alpha)}{2\Delta x},\\
b &= \frac{2}{\Delta t} v_s - v_s \frac{v_n - v_f}{2\Delta y} - g\frac{\eta_P^n - \eta_S^n}{\Delta y}\\
&\quad + \varepsilon \frac{v_n - 2v_s + v_f}{\Delta y^2} + B_y,
\end{aligned} \tag{29}$$

where α is given by Equation (25) and Pe_Δ is given by:

$$Pe_\Delta = \frac{u^* \Delta x}{\varepsilon} \quad \text{and} \quad u^* = \frac{u_w + u_e + u_s + u_{se}}{4}. \tag{30}$$

Similarly, for the second fractional time step, Equation (3) can be described by the following linear equations:

$$\begin{aligned}
a_P v_s^n &= a_N v_n^n + a_S v_f^n + b,\\
a_P &= \frac{2}{\Delta t} + \frac{2\varepsilon}{\Delta y^2} - C_y + \frac{v_s \alpha}{\Delta y},\\
a_N &= \frac{\varepsilon}{\Delta y^2} - \frac{v_s(1 - \alpha)}{2\Delta y},\\
a_W &= \frac{\varepsilon}{\Delta y^2} + \frac{v_s(1 + \alpha)}{2\Delta y},\\
b &= \frac{2}{\Delta t} v_s - u^* \frac{v_e - v_w}{2\Delta x} - g\frac{\eta_P^n - \eta_S^n}{\Delta y}\\
&\quad + \varepsilon \frac{v_e - 2v_s + v_w}{\Delta x^2} + B_y,
\end{aligned} \tag{31}$$

where α is given by Equation (25) and Pe_Δ is given by:

$$Pe_\Delta = \frac{v_s \Delta y}{\varepsilon}. \tag{32}$$

Equations (19), (20), (26), (27), (29), and (31) are solved using the tridiagonal matrix algorithm.

Sediment Transport and Morphological Module

Several mathematical models can describe the sediment transport due to the combined wave current outside the surf zone. However, inside the surf zone, the sediment transport process is very complicated because of wave breaking and induced turbulence. Even the most sophisticated models cannot simulate the sediment movement in this zone. Therefore, a simple empirical model is expected to yield comparable results with other sophisticated models after suitable calibration. The model described in this section calculates the total sediment transport loads by superimposing the separate transport loads due to waves and currents.

According to HORIKAWA (1988), WATANABE *et al.* (1986) developed a formula of the rate of transport due to mean current, which reads:

$$q_{cx} = Q_c u, \qquad q_{cy} = Q_c v,$$

$$Q_c = \frac{A_c(\tau - \tau_{cr})}{\rho g} = \frac{A_c(u_*^2 - u_{*cr}^2)}{g}, \tag{33}$$

where q_{cx} and q_{cy} are the transport loads in the x and y directions, respectively; u and v are the mean flow velocities in the x and y directions, respectively; $\tau_{\rm cr}$ and $u_{*\rm cr}$ are the critical shear stress and shear velocity, respectively; τ and u_* are the combined wave-current shear stress and shear velocity, respectively; and A_c is a dimensionless calibration coefficient (of the order 0.1~1).

Similarly, the sediment transport load due to wave motion can be obtained from WATANABE *et al*. (1984) as follows:

$$q_{wx} = F_d Q_w u_{bm} \cos\alpha, \qquad q_{wy} = F_d Q_w u_{bm} \sin\alpha,$$

$$Q_w = \frac{A_w(\tau - \tau_{cr})}{\rho g} = \frac{A_w(u_*^2 - u_{*cr}^2)}{g}, \tag{34}$$

where q_{wx} and q_{wy} are the transport loads in the x and y directions, respectively, A_w is a dimensionless calibration coefficient (of the order 0.1~1), and F_d is a direction function that defines the direction of the sediment transport load and smoothes the discontinuity at the null point (where the net transport is zero) (HORIKAWA, 1988). The direction function F_d is defined as:

$$F_d = \tanh\left(\kappa_d \frac{\Pi_c - \Pi}{\Pi_c}\right), \tag{35}$$

where κ_d is a coefficient that controls the degree of change in the cross-shore transport rate around the null point, the value of which is of the order of unity, and Π defines the direction of the sediment transport as follows:

$$\Pi = \frac{u_{bm}^2}{sgD}\frac{h}{L_0}\begin{cases} <\Pi_c & \text{onshore transport} \\ >\Pi_c & \text{offshore transport,} \end{cases} \tag{36}$$

where s is the specific gravity of the sediment grains and Π_c is a critical value of Π at the null point, which is expected to be of the order of unity. However, it must be determined empirically through trial computations (HORIKAWA, 1988).

A spatial distribution of sediment transport rates is estimated from local wave and current conditions according to Equations (33) and (34). The change in local bottom elevation z_b is calculated by solving the conservation equation of sediment mass, which reads:

$$\frac{\partial z_b}{\partial t} + \frac{\partial q_x}{\partial x} + \frac{\partial q_y}{\partial y} = 0.0, \tag{37}$$

where q_x and q_y are the total volumetric sediment transport rates in the x and y directions, respectively, and t is the time.

The formulas for sediment transport rates described above do not take into account the bottom slope. Therefore, even if a jagged profile resulted in the course of calculation with Equation (37), such that the local slope exceeded the repose angle of the sediment, the unrealistic steep slope could not be reduced (HORIKAWA, 1988). Although the wave-current field varies with beach transformation, the change of the flow field alone cannot be expected to completely suppress the creation of bottom jags.

In reality, when the local slope becomes steep, sediment grains tend to move downward owing to the force of gravity. In order to incorporate this effect, the following equation is used to calculate the change of bottom elevation (HORIKAWA, 1988):

$$\frac{\partial z_b}{\partial t} = -\frac{\partial}{\partial x}\left(q_x - \varepsilon_q|q_x|\frac{\partial z_b}{\partial x}\right) - \frac{\partial}{\partial y}\left(q_y - \varepsilon_q|q_y|\frac{\partial z_b}{\partial y}\right), \tag{38}$$

where ϵ_q is a positive constant determined empirically. Equation (38) corresponds to the use of the following modified sediment transport rates:

$$q_x' = q_x - \varepsilon_q|q_x|\frac{\partial z_b}{\partial x}, \qquad q_y' = q_y - \varepsilon_q|q_y|\frac{\partial z_b}{\partial y}. \tag{39}$$

Equation (38) is solved numerically using the finite difference method. A staggered mesh is employed in which the bottom elevation change z_b is calculated at the grid nodes and the transport loads are calculated at the grid faces.

Morphological Time Step

The value of the morphological time step is determined according to the rate of bed level change. The fastest bed change is associated with the smaller morphological time step and vice versa. After the model calculates the sediment transport fluxes, the absolute value of the rate of bed level change R is calculated for the whole domain using the sediment budget equation as:

$$R = \left|\frac{q_{xi,j} - q_{xi+1,j}}{\Delta x} + \frac{q_{yi,j} - q_{yi,j+1}}{\Delta y}\right|. \tag{40}$$

The morphological time step is then calculated from:

$$\Delta t_m = \min\left[\frac{h}{R}\left(\frac{\Delta h}{h}\right)\right] = \min\left(\frac{h}{R}\text{Accuracy}\right), \tag{41}$$

where $\Delta h/h$ is the ratio of the change in water depth at a certain point at the end of the morphological time step to the original water depth. This ratio is defined by the user at the desired accuracy. The smallest value of $\Delta h/h$ (higher accuracy) is related to the smallest morphological time step. The morphological time step is not allowed to extend beyond the duration of wave attack, where a different wave transformation is needed and consequently the hydrodynamics and the sediment transport rates will change. In addition, the morphological time step is not allowed to exceed the 50-day limit. In this way, the model will overcome the incorrect input of excessively large values of the accuracy by the user. On the other hand, for practical use of the model, the ratio $\Delta h/h$ should not be less than 5%.

Capabilities of the Model

Several model tests are performed to examine the ICEM capabilities for modeling the morphological changes in the vicinity of various coastal structures. The equilibrium beach profile concept is used to generate the initial beaches according to the median grain size D as follows (BRUUN, 1954):

$$h(x) = Ax^{2/3} \tag{42}$$

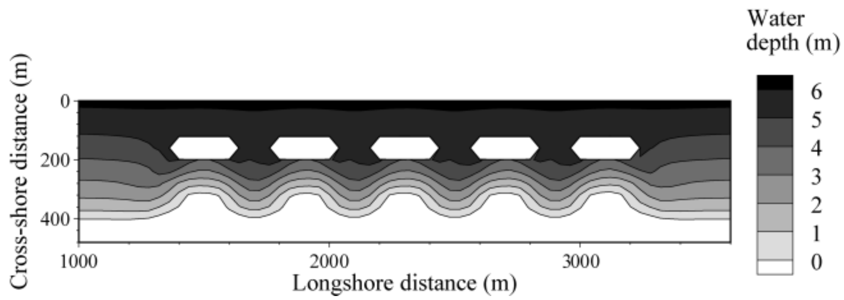

Figure 4. Morphological changes due to a system of detached breakwaters after 60 days.

where $h(x)$ is the water depth at distance x offshore and A is a dimensional scale parameter which is about 0.115 $m^{1/3}$ for sand of median grain size $D = 0.25$ millimeters (HERBICH, 1991).

Several configurations of coastal protection projects and their impact on the morphology of the seabed are tested. The first test is for a system of offshore breakwaters subjected to constant wave conditions. The system consists of five detached breakwaters of 200 meters length and 200 meters spacing. The breakwaters are located 240 meters from the shoreline. A perpendicular deep water wave of 2.0 meters significant height and 9.0 seconds significant period is assumed over 60 days. The morphological time step is calculated from Equation (41) assuming a 10% accuracy. Figure 4 shows the morphological impact of a system of detached breakwaters after 60 days, where the shoreline advances behind the breakwaters in the form of large salients. As the salients advance toward the breakwaters, it is expected that the circulation cells behind the breakwaters will get smaller and stronger. Therefore, the rate of change of the salient's geometry continuously changes with time. Figure 5 shows an example of the wave driven currents formed behind the system of breakwaters after 28 days. It can be seen that significant changes of the hydrodynamics occur as a result of the bathymetric changes. In addition, the source of sediments that build up the salients is from the vicinity of the breakwaters, as shown in Figure 5. Therefore, the salients' build up is accompanied by offshore erosion between the breakwaters as shown in Figure 4.

In cases where the waves are predominantly attacking the beach at large oblique angles, the groin system is very common. The same sandy beach used in the previous case is used. A constant deep water wave climate of 1.5 meters significant height and 9.0 seconds significant period is assumed. A large offshore wave angle ($\theta_0 = 45°$) is used to derive a significant amount of littoral drift so that the groins' effect is signified. The system is composed of four groins of 200-meter length and spaced at 600 meters, which corresponds to three times the groin length. Figure 6 shows the morphological impact of the groin system on the beach after 90 days. Figure 7 shows the circulation around the groin system after 60 days, where the bathymetric impacts on the circulation around the groin system are evident. The littoral drift is diverted by the groin system as shown in Figure 7, which causes significant offshore bathymetric changes around each groin, as shown in Figure 6. A submerged groin system is expected to cause less littoral drift diversion than the emerged groin system and therefore less morphological impact in the offshore. Figure 8 shows the circulation around a submerged groin system of similar length and spacing. The groins are 1.5 meters above the bed. It is shown that the submerged system does not divert the littoral transport as much as the emerged system does. Therefore the impact of the submerged system on the offshore part of the beach is less than the emerged groin system as shown in Figure 9.

The simulation results for the above test cases show the realistic behavior of the ICEM and demonstrates its ability to simulate morphological changes around coastal structures.

RAS EL-BAR CASE STUDY

The Nile Delta coast, on the Mediterranean Sea, was formed through many centuries. The continuous discharge of

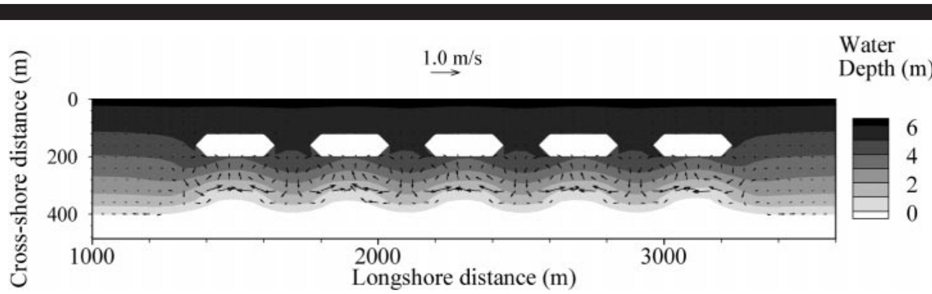

Figure 5. Circulation behind the detached breakwaters (after 28 days).

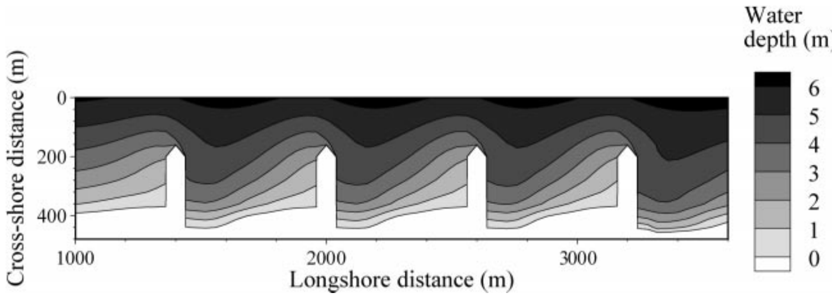

Figure 6. Morphological changes due to a system of impermeable groins (after 90 days of wave action).

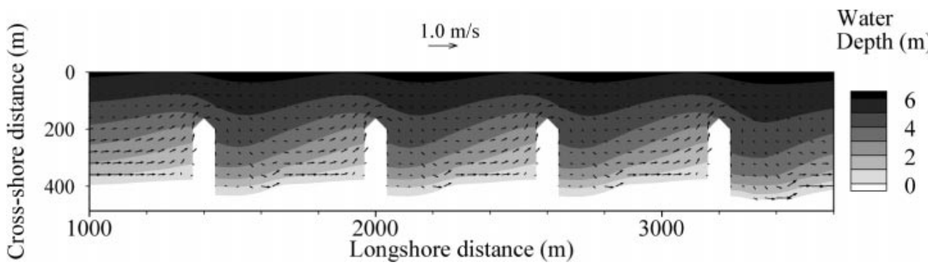

Figure 7. Circulation around a system of impermeable groins (after 60 days).

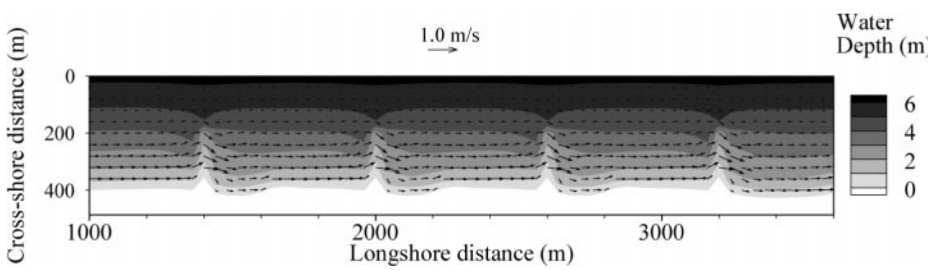

Figure 8. Circulation around a system of submerged groins (after 70 days).

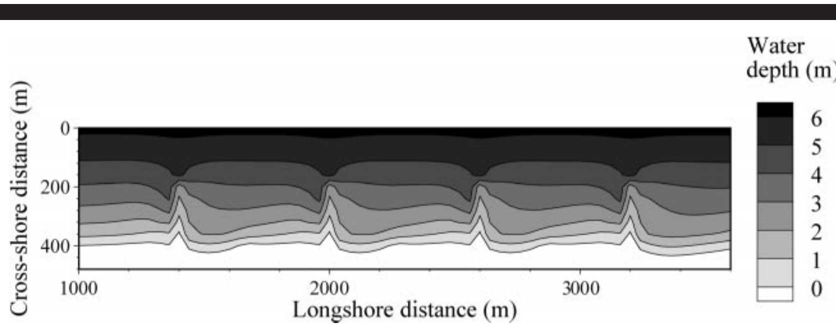

Figure 9. Morphological changes due to a system of submerged groins (after 90 days of wave action).

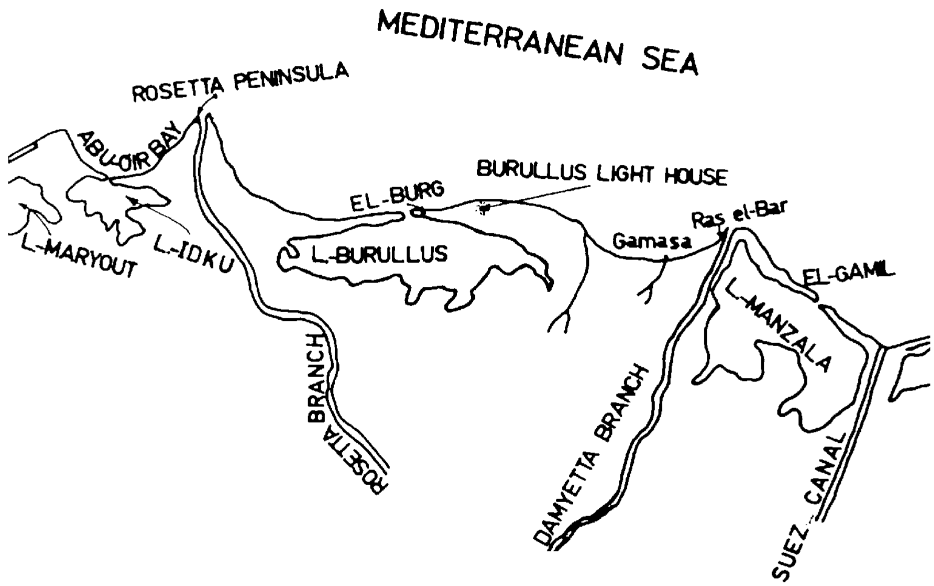

Figure 10. The Nile Delta and Ras El-Bar area (Mobarek, 1972).

large quantities of sediments from the Nile into the Mediterranean over thousands of years formed two peninsulas in the sea at the two main branches of the Nile, *i.e.,* Rosetta and Damietta, as shown in Figure 10. In the course of time, the supply of sediment by the Nile exceeded the loss due to wave and current action, resulting in a continuous advance of the shoreline towards the sea (MOBAREK, 1972). This process continued until the erosive wave action and the continuous supply of sediment materials reached a stable condition. By the end of the 18th century and the start of the 19th century, several regulation projects along the River Nile had been constructed, which reduced the sediment supply from the Nile to the Mediterranean and erosion from Rosetta and Damietta peninsulas was observed. After the construction of the High Dam in 1964, the sediments carried out to the Nile Delta were significantly reduced. After the completion of the Faraskour Dam, at the end of Damietta promontory, the supply of the River Nile water to the Mediterranean has been completely cut off. Accordingly, the River Nile lost stability with Mediterranean and severe erosion was observed.

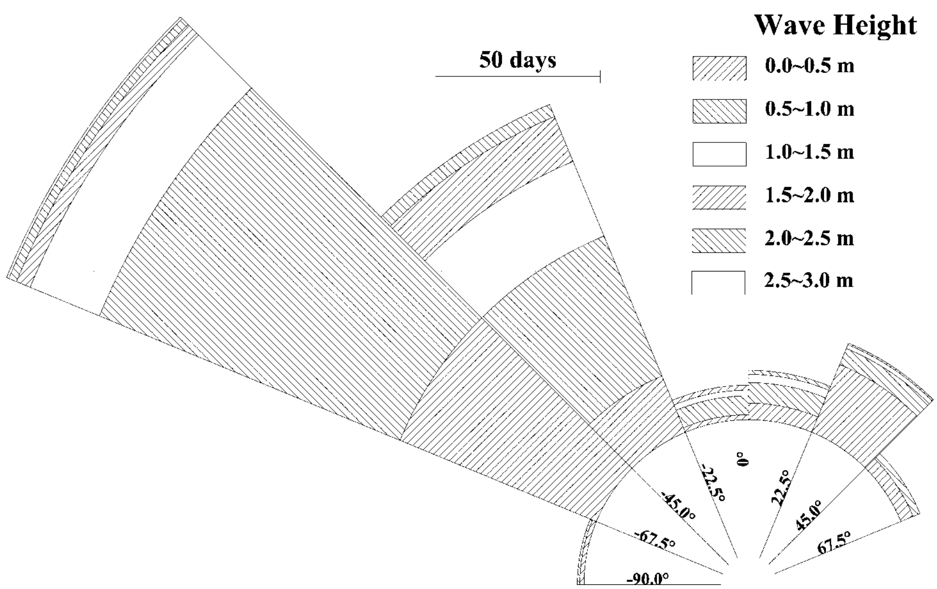

Figure 11. Wave rose at Ras El-Bar.

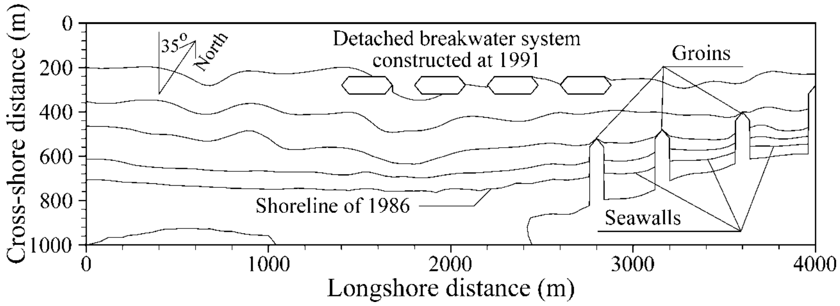

Figure 12. Schematic diagram of the modeled region.

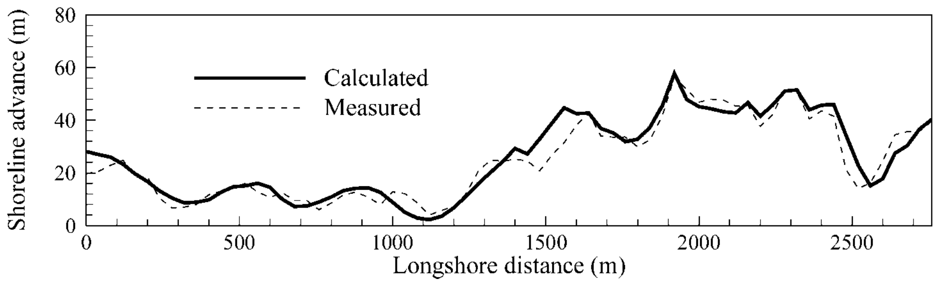

Figure 13. Shoreline advance from 1986 to 1993 (measured and calculated).

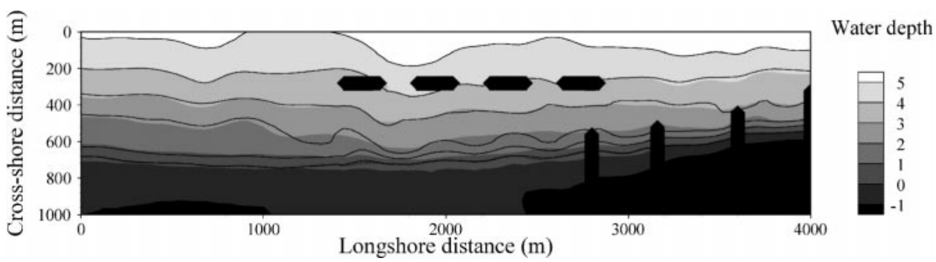

Figure 14. Ras El-Bar in November 1986 and July 1993 (measured and calculated). Gray scale represents the initial contour map of 1986. Contour lines represent the deformed beach at 1993. Thick dotted line represents the measured shoreline at 1993.

The city of Ras El-Bar, located west of Damietta Nile branch as shown in Figure 10, depicts this instability. Severe erosion has been recorded at Ras El-Bar since 1895. It is reported that between 1902 and 1940, the Damietta Peninsula receded about 1.8 kilometers (MOBAREK, 1972). Therefore, several coastal protection projects have been implemented to reduce or eliminate the erosion. The west (terminal) jetty was constructed in 1941; three groins were constructed in 1970, and the beach was artificially nourished with sediments dredged from the river mouth (FRIHY *et al.,* 1991). A dolos and riprap revetment was placed within the groin field (DABEES and KAMPHUIS, 1998). Erosion continues beyond the western groin, progressively diminishes to the west, and is negligible along the western half of Ras El-Bar (FRIHY *et al.,* 1991). A system of detached breakwaters was constructed in 1990 west of the groin field (DABEES and KAMPHUIS, 1998). The breakwaters were placed 400 meters offshore such that the tombolo formation is prevented. In 1994, the beach was nourished with 200,000 cubic meters of sand. The Ras El-Bar beach is composed of silty sand with a median diameter of 0.12 millimeters (MOBAREK, 1972).

Data Analysis and Model Setup

The time series wave data over a complete representative year at Ras El-Bar is available from the Coastal Research Institute, Alexandria, 1996 (DABEES and KAMPHUIS, 1998). The significant wave data are given every 6 hours. The wave gauge was located at the eastern side of Damietta promontory 7 meters below the water (DABEES and KAMPHUIS,

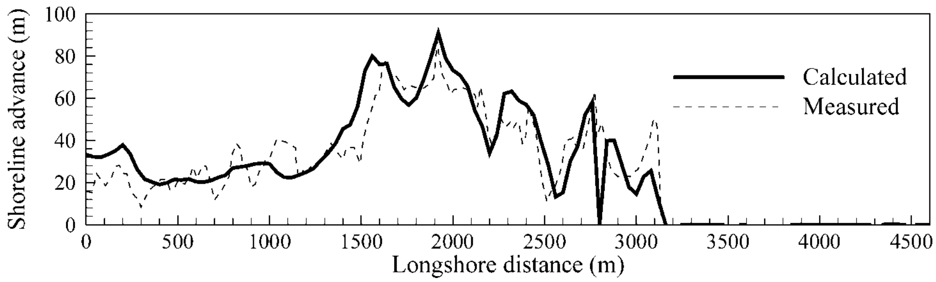

Figure 15. Shoreline advance from 1986 to 1995 (measured and calculated).

1998). Figure 11 shows the annual wave rose at Ras El-Bar. Over the year, only 240 days were considered, where the wave heights are larger than 0.75 meters. The monthly wave rises were analyzed in order to come out with a design time series. It was assumed that over 1 month short-duration storms that have the same range of wave heights can be grouped into a single prolonged storm.

The study was conducted in three main phases. The first phase is from 1986 to 1991 before the construction of the detached breakwaters. The second and third phases study the effect of the detached breakwaters from 1991 until 1993 and 1995, respectively.

The same coordinate system and modeled region used by DABEES and KAMPHUIS (1998) is adopted in this study. The modeled region covers 4 kilometers of beach and 1 kilometer offshore from an arbitrary baseline. Figure 12 shows a schematic diagram of the modeled region and the existing structures, as well as the initial contour map of November 1986.

Measured shorelines of 1986, 1993, and 1995 were digitized from DABEES and KAMPHUIS (1998), and the initial bathymetry was digitized from HERBICH *et al.* (1996).

Model Calibration and Verification

The model is calibrated and verified using the measured shorelines of 1993 and 1995, respectively. The morphological model parameters described above are adjusted beforehand so that winter and summer profiles are formed appropriately. Using the average wave conditions (H_s = 1.0 meters and T_s = 7.5 seconds), the parameters A_c and A_w are set approximately to reproduce the 1993 shoreline. The actual wave climate is then used over the period from November 30, 1986 to July 1, 1993 (phase 1 and 2), where the calculated shoreline is compared with the actual shoreline to fine tune the calibration parameters. The optimized values of the calibration parameters A_c, A_w, κ_c, κ_d, and Π_c for the Ras El-Bar area are 0.11, 0.15, 1.0, 0.2, and 2.0, respectively. Figure 13 shows the measured and computed shoreline advance from 1986 to 1993 after calibration. The error in the total shoreline advance is less than 5%. Figure 14 shows the measured and calculated shorelines of 1993 after calibration as well as the initial bathymetry at 1986. It can be shown that the seabed erodes in the vicinity of the detached breakwater system. This is due to the circulation cells formed behind the breakwaters, which move the sediments from the breakwaters' vicinity to the shore, where they settle down and build up salients as shown in Figure 14. On the other hand, the beach slope in front of the seawalls continues steeping due to the offshore transport of sediments generated by the wave action.

In order to verify the model, the same parameters are used to calculate the 1995 shoreline. Figure 15 shows the measured and computed shoreline advance from 1986 to 1995. Again, the error in the total shoreline advance is less than 5%. Figure 16 shows the morphological changes after phase 3. Like phase 2, erosion in the vicinity of the detached breakwater system is reported. At 1995, the overall beach profile seems to reach steady state. Significant erosion occurs behind the first breakwater from the west, which suggests some kind of toe protection.

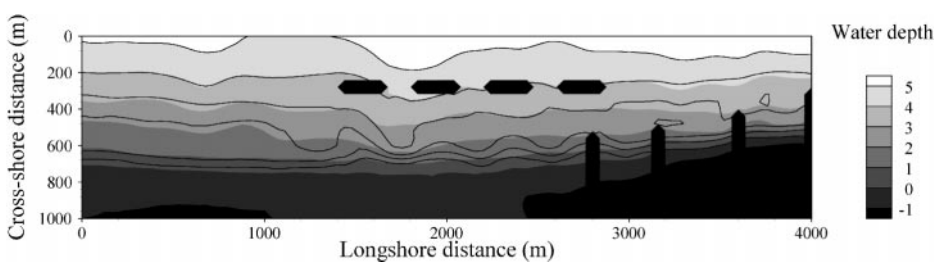

Figure 16. Ras El-Bar in November 1986 and July 1995. Gray scale represents the initial contour map of 1986. Contour lines represent the deformed beach in 1995.

CONCLUSION

The proposed three-dimensional morphodynamical model can be used for long-term shoreline predictions. In addition, it can be used as a design tool for coastal protection structures since its applicability is proven for both the long and short term. Unlike one-line models, the three-dimensional model can be used to predict the morphological changes in the vicinity of coastal structures, which gives critical information that may affect their structural design structures. The ICEM was successfully applied to the Ras El-Bar area, which has several erosion control structures. When compared with the field measurements, the model results are considered to be very good.

ACKNOWLEDGMENT

We thank Dr. Mohamed Dabees for providing us with the necessary wave data for the Ras El-Bar area.

LITERATURE CITED

BERKHOFF, J.C.W., 1972. Computation of combined refraction-diffraction. *Proceedings of the 13th Coastal Engineering Conference,* Vancouver, British Columbia, ASCE, Vol. 1, pp. 471–490.

BROKER, I., 1995. Coastal area modelling. *MAST 68-M Final Workshop,* Gdansk, Poland, pp. 2-86 to 2-90.

BROKER, I.; JOHNSON, H.K.; ZYSERMAN, J.A.; RONBERG, J.K.; PEDERSEN, C.; DEIGAARD, R., and FREDOSE, J., 1995. Coastal profile and coastal area morphdynamic modelling. *MAST 68-M Final Workshop,* Gdnask, Poland, pp. 7-12 to 7-16.

BRUUN, P., 1954. Coast erosion and the development of beach profiles, Beach Erosion Board, Tech. Memo. No. 44. U.S. Army Corps of Engineers.

DABEES, M., and KAMPHUIS, J.W., 1998. ONELINE, A numerical model for shoreline change. *Proceedings of the 26th International Conference of Coastal Engineering,* pp. 2668–2681.

DALLY, W.R., and OSIECKI, D.A., 1994. The role of rollers in surf zone currents. *24th International Conference on Coastal Engineering,* Kobe, Japan, pp. 1895–1905.

DE VRIEND, H.J.; ZYSERMAN, J.; NICHOLSON, J.; ROELVINK, J.A.; PECHON, P., and SOUTHGATE, H.N., 1993. Medium-term 2DH coastal area modelling. *Coastal Engineering,* 21, 193–224.

FRIHY, O.E.; FANOS, A.M.; KHAFAGY, A.A., and KOMAR, P.D., 1991. Patterns of nearshore sediment transport along the Nile Delta, Egypt. *Coastal Engineering,* 15, 409–429.

HERBICH, J.B. (ed.), 1991. *Handbook of Coastal and Ocean Engineering.* Houston, Texas: Gulf Publishing Co.

HERBICH, J.B.; ELFIKY, A.; ELMONGY, A.; ELBAHRAWY, A., and EL-SAEED, G., 1996. Shore protection studies for Ras-Elbar, Egypt. *Proceedings of the 25th International Conference of Coastal Engineering,* ASCE, pp. 3976–3985.

HORIKAWA, K., 1988. *Nearshore dynamics and coastal processes.* Tokyo, Japan: University of Tokyo Press.

LE BLOND, P.H., and TANG, C.L., 1974. On energy coupling between waves and rip currents. *Journal of Geophysical Research,* 79(6), 811–816.

LEONT'YEV, I.O., 1999. Modeling of morphological changes due to coastal structures. *Coastal Engineering,* 38, 149–166.

LONGUET-HIGGINS, M.S., 1970. Longshore currents generated by obliquely incident sea waves, Parts 1 and 2. *Journal of Geophysical Research,* 75(33), 6778–89, 6790–6801.

MOBAREK, I.E., 1972. The Nile Delta Coastal Protection Project. *Proceedings of the 13th Coastal Engineering Conference,* ASCE, Vol. 2, pp. 1409–426.

PRICE, D.M.; CHESHER, T.J., and SOUTHGATE, H.N., 1995. *PISCES: A Morphological Coastal Area Model.* Report SR 411. Wallingford, U.K. HR Wallingford.

ROELVINK, J.A.; RENIERS, A.J.H.M., and WALSTRA, D.J.R., 1995. Medium term morphodynamic modelling. *MAST 68-M Final Workshop,* Gdnask, Poland, pp. 7-3 to 7-6.

SAIED, U., and TSANIS, I.K., 2004. Improved boundary equations for elliptic water wave models. *Coastal Engineering,* 51(1), 17–34.

SAIED, U.M., and TSANIS, I.K., 2005. Improved parabolic water wave transformation model. *Coastal Engineering,* 52(2), 139–149.

SHEN, H., 1991. Numerical Analysis of Large-Scaled Flows and Mass Transports in Lakes. Kyoto, Japan: Kyoto University, Ph.D. thesis, 273p.

WATANABE, A.; MARUYAMA, K.; SHIMIZU, T., and SAKAKIYAMA, T., 1984. Numerical prediction model of three-dimensional beach deformation around coastal structures. *Proceedings of the 17th Coastal Engineering Conference,* ASCE, pp. 1106–1121.

WATANABE, A.; MARUYAMA, K.; SHIMIZU, T., and SAKAKIYAMA., T., 1986. Numerical prediction model of three-dimensional beach deformation around a structure. *Coastal Engineering in Japan,* 29, 179–194.